Electron-impact excitation of the $1\,^1S \rightarrow 3\,^1P$ and $1\,^1S \rightarrow 4\,^1P$ transitions in helium

M. A. Khakoo, D. Roundy,* and F. Rugamas
Physics Department, California State University, Fullerton, California 92634
(Received 20 February 1996)

The method of electron-photon coincidence is used to ''resolve'' the electron-impact excitation of the $n\,^1P$ levels ($n=3$ and 4) from nearby levels. Experimentally determined ratios of the differential cross sections for the electron-impact excitation of $1\,^1S \rightarrow 2\,^1P$, to $1\,^1S \rightarrow 3\,^1P$, and $4\,^1P$ transitions are presented at 30-, 40-, and 80-eV incident electron energies. Differential cross sections for the $1\,^1S \rightarrow 3\,^1P$ and $1\,^1S \rightarrow 4\,^1P$ transitions are derived by normalizing these ratios to available experimental differential cross sections for the $1\,^1S \rightarrow 2\,^1P$ transition. The ratios and differential cross sections are compared to available theoretical and semiempirical data. [S1050-2947(96)06210-5]

PACS number(s): 34.10.+x, 34.80.Dp

I. INTRODUCTION

Considerable effort has been made in the past to investigate the electron-impact excitation of helium. Despite its relatively simple electronic structure, helium continues to be a very important target for electron-scattering studies for numerous reasons. Pioneering studies of the fundamental processes in electron collisions, e.g., elastic electron scattering, electron-impact excitation, resonant electron scattering, ionization (including e-$2e$), etc. have been carried out using helium as a target. The studied electron-helium scattering processes, in turn, have found widespread applications in man made plasmas (e.g., in Penning-ionization spin-polarized electron sources or as a buffer gas or in helium-filled lasers). In addition, helium is an abundant element and, therefore, helium emissions are widely observed in a variety of stellar and interstellar media, and are in turn used for determining abundances of this element. It is, therefore, important to provide quantitative electron collision cross sections for this target. Differential scattering electron-energy-loss spectroscopy (EELS) has yielded a significant quantity of data concerning both elastic and inelastic electron-scattering channels [1]. Using conventional EELS, differential cross sections for the excitation of the strong $1\,^1S \rightarrow n\,^1P$ transitions in helium have been possible, but have been limited to the energetically resolvable $1\,^1S \rightarrow 2\,^1P$ transitions where some of the most accurate inelastic differential-cross-section (DCS) measurements are to be found [2]. There is also a significant body of data concerning coherence and correlation parameters for the excitation of the $2\,^1P$ and the $3\,^1P$ levels [3,4]. No absolute experimental differential cross sections (DCS's) are available for the excitation of the $n\,^1P$ levels ($n>2$), the reason being that conventional EELS from gaseous targets (employing electron beams of intensity of several nA) cannot provide the high-energy resolution (<13 meV) required to resolve the $3\,^1P$ and $4\,^1P$ levels from close-by levels, as well as providing adequate scattered electron signal for precise DCS measurements.

A semiempirical attempt [5] to obtain DCS's for the $n=3$ levels using EELS, used first-order many-body theory (FOMBT) to calculate the contribution, to the signal, from the $1\,^1S \rightarrow 3\,^1D$ and $3\,^3D$ transitions. Since this effort relied on theory, it is useful to attempt to determine these DCS's by a direct method.

For excitation of the $1\,^1S \rightarrow n\,^1P$ transitions in helium, there has been a considerable amount of activity on the theoretical front. Earlier, an 11-state R-matrix calculation [6] was used in astrophysical investigations [7] aiming to determine the H:He ratios of primordial regions of the universe. Subsequently, 19- and 29-state calculations have been made [8]. Even more recently, a theoretical (FOMBT) and experimental collaboration has resulted in two papers regarding the electron-impact excitation of the $1\,^1S \rightarrow n\,^1P$ transitions in helium [9]. Also, the very recent convergent close-coupling method [10] (CCC) has been very successful when applied to electron scattering from targets whose wave functions are relatively simple, e.g., hydrogen, helium, and sodium. Fully experimental DCS's for the $1\,^1S \rightarrow 3\,^1P$, $4\,^1P$ transitions are thus desirable as tests for present theories.

In addition, there is interest regarding the n dependence of these DCS's for the $1\,^1S \rightarrow n\,^1P$ transitions. Cartwright and Csanak [11], showed in the context of the FOMBT, that for helium the $1\,^1S \rightarrow n\,^1P$ electron-impact excitation transition matrix elements are strongly dependent on the radial (r) part of the wave function close to the nucleus. This idea is also expounded by Bubelev *et al.* [12]. In the case of helium the $n\,^1P$ wave functions show essentially identical form for small r. Thus factoring out the r terms in these transition matrix elements results in the following.

(i) Various ratios of the magnetic sublevel transition matrices become independent of n.

(ii) $1\,^1S \rightarrow n\,^1P$ excitation cross sections should scale in proportion to $(n-\mu_n)^{-3}$, where μ_n is the quantum defect associated with the $n\,^1P$ level. Thus $1\,^1S \rightarrow n\,^1P$ ($n>2$) cross sections can be derived from $1\,^1S \rightarrow 2\,^1P$ cross sections.

(iii) The electron-photon coherence and correlation parameters [3] for an excited state of particular symmetry can be determined accurately by measurements for the strong $1\,^1S \rightarrow n\,^1P$ transition, and using these measurements as also representing those of the other $1\,^1S \rightarrow n\,^1P$ ($n>2$) transitions which have lower electron scattering cross sections.

*Permanent address: Physics Department, U.C. Berkeley, Berkeley, CA 94720.

This was demonstrated experimentally by Hammond, Khakoo, and McConkey [13], the data being restricted to an incident energy of 80 eV and a scattering angle of 20°. As previously stated, the $n\,^1P$ n-independence model was further discussed very recently by Bubelev *et al.* [12], who applied it to electron-hydrogen, electron-sodium, and positron-helium scattering using the distorted-wave Born approximation (DWBA).

In this work, an extension of an earlier report [14], we present direct DCS measurements of excitation cross sections for the $1\,^1S \rightarrow n\,^1P$ ($n=3$ and 4) transitions in helium, based on the electron-photon coincidence method.

II. SCHEME OF MEASUREMENT

The present measurements determine the ratios R_{nP} of the DCS's $[d\sigma/d\Omega_e(E_0,\theta_e)_{nP}]$ for the electron-impact excitation of the $1\,^1S \rightarrow n\,^1P$ ($n=3$ and 4) transitions. We define these ratios as

$$R_{nP}=\frac{d\sigma/d\Omega(E_0,\theta_e)_{2P}}{d\sigma/d\Omega(E_0,\theta_e)_{nP}} \tag{1}$$

at a given incident electron energy (E_0) and scattering angle (θ_e). Using these ratios, the DCS's for the $1\,^1S \rightarrow n\,^1P$ transition may be determined by normalization of R_{nP} to the experimental DCS's for the $1\,^1S \rightarrow 2\,^1P$ which are available [9,15,16,24]. The electron-photon coincidence method is used to separate out the electron-impact excitation channel for the $1\,^1S \rightarrow n\,^1P$ ($n=3$ and 4) transitions from other excitation channels present in conventional EELS spectra of helium.

A. Theory

The experimental determination of R_{nP} using the electron-photon coincidence technique in helium relies on the fact that the helium atomic levels are fully LS coupled. Thus in excitation of the singlet→singlet transitions by electrons, spin interactions are negligible and can be factored out. Additionally, parity conservation in electromagnetic interactions restricts the excited-state charge distribution $\langle n\,^1P|n\,^1P\rangle$ to have the same reflection symmetry (+ with respect to the scattering plane) as the ground state (isotropic) charge distribution $\langle n\,^1S|1\,^1S\rangle$. The excited $n\,^1P$ state in the natural frame coordinates (Fig. 1) can now be written as [3]

$$|n\,^1P\rangle = f^n_{-1}|1,-1\rangle + f^n_1|1,1\rangle, \tag{2}$$

where f^n_{-1} and f^n_1 are the (complex) scattering amplitudes describing the excited state in the $|L,m_L\rangle$ orbital basis ($L=1$, $m_L=1$, 0, -1) with the axis of quantization perpendicular to the scattering plane.

Using the geometry in Fig. 1, the electron-photon coincident rate, dN_c/dt, for any transition can be written as [17]

$$dN_c/dt = d\sigma/d\Omega_e(E_0,\theta_e) \times\{I_e N_G L_e \Delta\Omega_e \Delta\Omega_\gamma\} E_e E_\gamma \beta_\gamma \zeta(\theta_\gamma,\Phi_\gamma). \tag{3}$$

Here I_e, N_G, L_e, $\Delta\Omega_e$, and $\Delta\Omega_\gamma$, respectively, are the incident electron fluence (s^{-1}), target gas number density (cm^{-3}), ''effective'' path length of electrons through the gas target beam (cm), electron analyzer, and photon detector solid angles (sr). E_e and E_γ are the respective detection efficiencies for electrons and photons, and β_γ is the branching ratio for the observed radiation. Again, $d\sigma/d\Omega_e$ is the excitation DCS ($cm^2\,sr^{-1}$). $\zeta(\theta_\gamma,\Phi_\gamma)$ is the normalized angular distribution function of coincident photons which contains the geometric information of the excited state charge cloud. For the fully LS coupled $1\,^1S \rightarrow n\,^1P$ transitions in helium at a fixed θ_e [3]

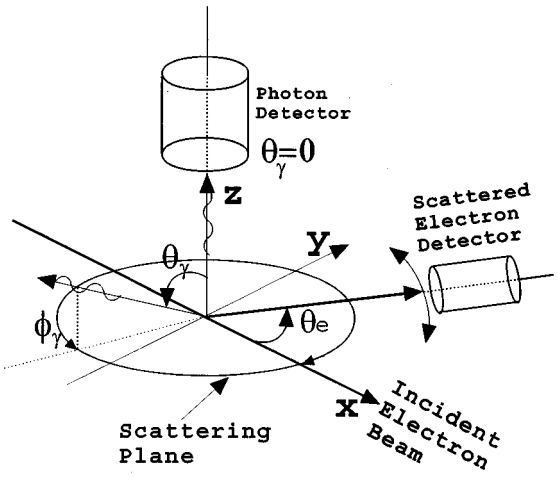

FIG. 1. The scattering geometry for the present electron-photon coincidence experiment, shown in the ''natural'' frame [3].

$$\zeta(\theta_\gamma,\Phi_\gamma) = \tfrac{1}{2}(3/8\pi)[1+\cos^2\theta_\gamma - P_L \times \cos 2(\Phi_\gamma-\gamma)\sin^2\theta_\gamma] \tag{4}$$

(θ_γ and Φ_γ are the polar coordinates of the photon detector) with $P_L=2|f^n_1||f^n_{-1}|$ and $\langle f^n_1 f^{n*}_{-1}\rangle = -\tfrac{1}{2}P_L \exp(-2i\gamma)$. γ is the alignment angle of the excited state charge distribution [3]. When $\theta_\gamma=0$, i.e., the photons are observed perpendicular to the scattering plane, as in the present case (see Fig. 1), $\zeta(0,\Phi_\gamma)=3/8\pi$ and the coincidence rate given by Eq. (3) is directly proportional to the excitation DCS $d\sigma/d\Omega_e(E_0,\theta_e)$ if the photon detector is polarization insensitive. If this is not the case then coincident measurements should be taken at two orthogonal values of Φ_γ, and then summed.

Our method is to take such electron-photon coincidence spectra for the $\theta_\gamma=0$ setup, for the $1\,^1S \rightarrow 2\,^1P$, $1\,^1S \rightarrow 3\,^1P$, and $1\,^1S \rightarrow 4\,^1P$, transitions in helium under identical conditions [identical parameters in { } in Eq. (3)] and known respective times Δt_{2P}, Δt_{3P}, and Δt_{4P}. Corrected for detector efficiencies, the averaged coincidence rate $\{N_c(2P)/\Delta t_{nP}\}(E_0,\theta_e)$ ($n=2$, 3, and 4) obtained from the coincidence spectra yield the ratios

$$\frac{\{N_c(2P)/\Delta t_{2P}\}(E_0,\theta_e)}{\{N_c(nP)/\Delta t_{nP}\}(E_0,\theta_e)} = \frac{d\sigma/d\Omega(E_0,\theta_e)_{2P}}{d\sigma/d\Omega(E_0,\theta_e)_{nP}} = R_{nP} \tag{5}$$

from Eq. (3), where N_c (nP) is the accumulated number of coincidences for the feature nP in the acquisition time Δt_{nP}, etc. We note that this equation applies even when the photon detector solid angle is finite, but centered about $\theta_\gamma=0$ as can be observed by integrating $\zeta(\theta_\gamma,\Phi_\gamma)$ about a cone centered

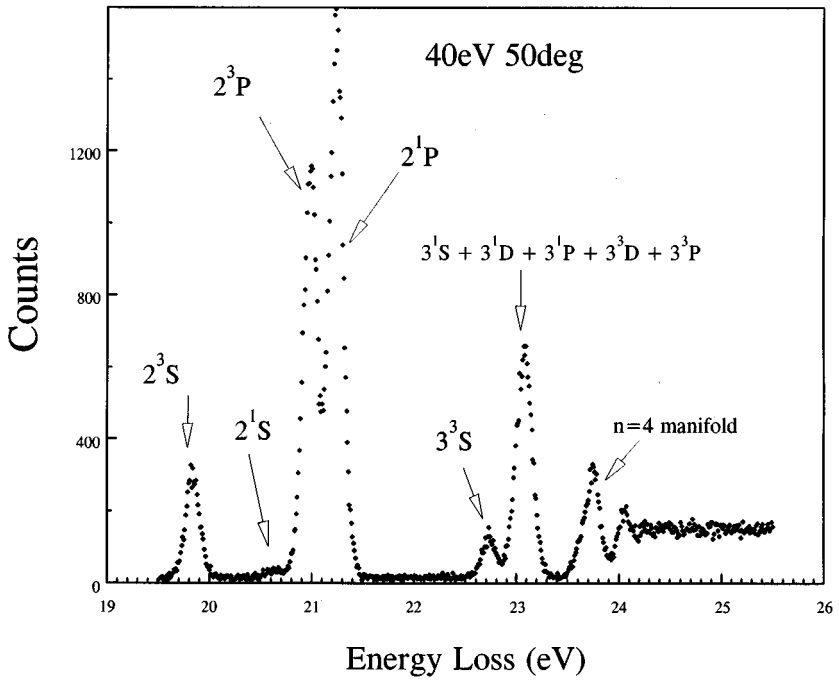

FIG. 2. EELS spectrum of helium taken at 40-eV 50°, showing the situation regarding resolution of features by our electron beam. The FWHM energy resolution is about 160 meV, and the incident electron current is 0.4 uA.

about $\theta_\gamma=0$. These R_{nP} ratios can be used to determine the DCS for the n^1P feature using the 2^1P DCSs from a conventional EELS experiment.

B. Experimental setup and measurements

In our setup, a monochromated electron beam crosses a gas jet from a molybdenum needle. Scattered electrons are detected as a function of energy loss (ΔE) and θ_e by a hemispherical analyzer equipped with a high count-rate, long-life electron multiplier ETP model AF151H). The electron spectrometer has virtual apertures of 1.5-mm diameter and an energy resolution varying from 120 to 200 meV, an angular resolution of 5° full width at half maximum (FWHM) with an incident electron current in the range of 0.1 to 0.7 μA. Its θ_e setting is computer controlled via a stepper motor placed outside the vacuum. A typical electron-energy-loss spectrum taken by this instrument is shown in Fig. 2. Perpendicular to the scattering plane is the vacuum-ultraviolet (VUV) photodetector (an electron multiplier with aluminium dynodes, ETP AF151) which has three 91% transparency molybdenum grids. The first (i.e., nearest to collision region) and third are shorted to the collision region, and the second is at +1.5 V (relative to the collision region) to repel helium ions. The first dynode of the photodetector is at $-E_0-5$ V (relative to the collision region) to repel electrons from reaching it. The photodetector dynode area was 0.8 cm^2, and placed 2.8 cm from the collision region. In the preliminary stages of this experiment an in-vacuum stepper motor was used to rotate the photodetector about the angle Φ_γ (Fig. 1) to determine its polarization efficiency, but was later removed (see Sec. III). The helium gas jet is angled at ≈45° relative to the scattering plane to shoot the thermal beam of helium downwards in an effort to reduce the detection of neutral helium $2\,^1S$ or $2\,^3S$ metastables by the photomultiplier. We estimated that the metastable signal was <5% of the total photon signal. The timing response and count-rate performance of the photomultiplier were <10 ns (pulse width, FWHM), a jitter time of ≈1 ns, and an observed linearity in count rate in the range up to and greater than 200 kHz. The type of detectors (electron and photon detectors) used here proved crucial to the experiment, since they did not need rejuvenating like conventional channel electron multipliers, and we could acquire data for essentially indefinitely long periods even at high count rates.

The vacuum was maintained by an unbaffled Diffstak pump (Edwards High Vacuum) with Santovac oil, backed by a rotary pump using a low-grade diffusion pump oil (Diffoil 20, K.J. Lesker Co., vapor pressure ≈10^{-7} torr) and equipped with a Micromaze (K.J. Lesker Co.) oil vapor trap. The base pressure of the vacuum tank was typically 6×10^{-8} torr.

The electron spectrometer has been discussed previously [18]. The experiment was baked using biaxial heaters (Ari Industries Inc.) at 120 °C (including the detectors) to stave off the long-term deleterious effects of diffusion pump oil, and performed stably for periods of greater than nine months. Typical count rates varied from ≈10 to ≈2 kHz in the photon channel, and ≈100 khz to 50 Hz in the electron channel. The detectors were connected to fast preamplifiers (EG&G Ortec Model VT120), and then to a modern coincidence system using constant fraction discriminators, a time-to-pulse height converter (TPHA) and an analog-to-digital converter (ADC). The ADC (Accuspec Na I board, Canberra Instruments) was part of an IBM personal computer which controlled the two stepper motors (θ_e and Φ_γ) in the experiment, monitored the pressure behind the gas source and the voltages in the experiment (e.g., energy losses) via a multiplexer system, and reset the ADC for different coincidence spectra, keeping track of number of repetitive loops, standard deviation drifts in gas pressure, electron current (if needed), electron-energy-loss voltages, etc. The electron channel was used to start the TPHA. The gas source drive pressure was

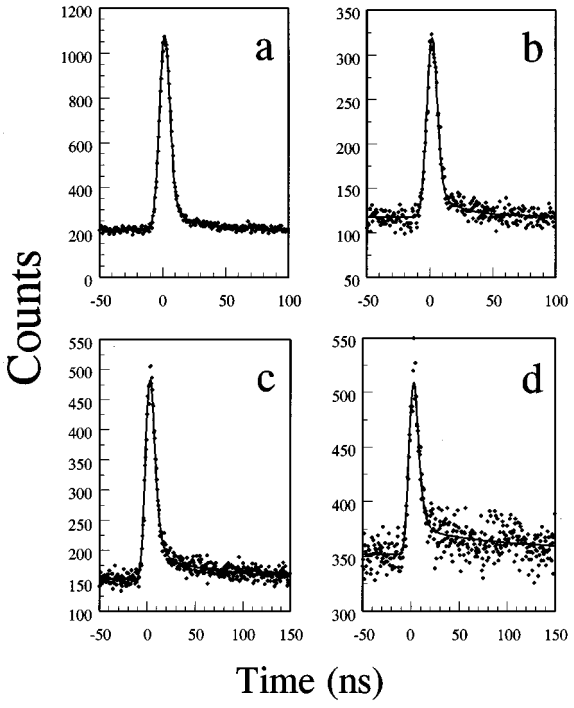

FIG. 3. Selection of fitted electron-photon coincidence spectra at $E_0=40$ eV and various θ_e. (a) $3\,^1P$ coincidence spectrum at $E_0=40$ eV and $\theta_e=20°$. (b) Same as (a), but at 100°. (c) $4\,^1P$ coincidence spectrum at $E_0=40$ eV and $\theta_e=10°$. (d) Same as (c), but at 50°.

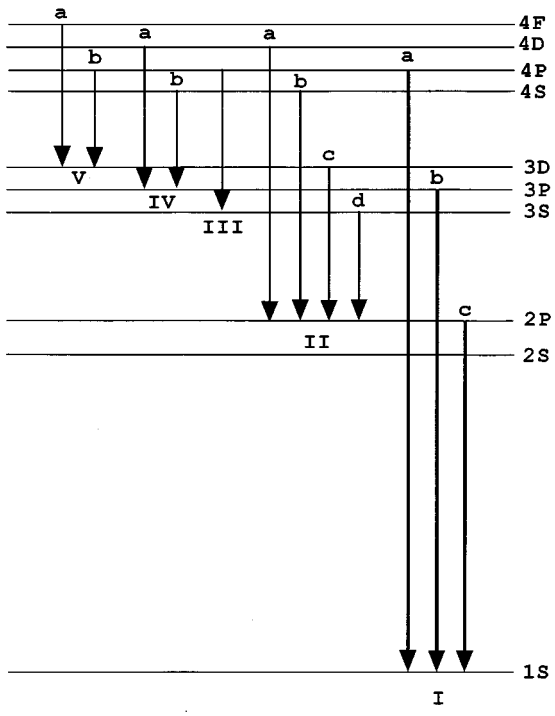

FIG. 4. Energy-level diagram of pertinent helium *singlet* states involved in observed photons and important cascade routes.

kept below 1.0 torr and this closely corresponded linearly to a pressure of below 1×10^{-6} torr in the experimental chamber (corrected for the sensitivity of the ionization gauge).

After tuning the electron spectrometer to achieve as best as possible the desired flat ionization energy loss profile [19] at 30-eV impact energy (to obtain a uniform analyzer transmission), the following procedure was used to set up the system for coincidence: We scanned an energy-loss spectrum at the fixed E_0 and θ value and then located the maximum of the $2\,^1P$ from the $2\,^3P$ levels (e.g., see Fig. 2). At large angles, this had to be determined by unfolding the nearby levels using a spectrum fitting program that we have, which was discussed by Khakoo *et al.* [20]. Having centered the energy-loss setting of the spectrometer for the $1\,^1S \rightarrow 2\,^1P$ feature, the computer was set to go repetitively to additional energy losses of 0, +1.8685, and 2.523 eV, for the $1\,^1S \rightarrow 2\,^1P$, $1\,^1S \rightarrow 3\,^1P$, and $1\,^1S \rightarrow 4\,^1P$ features. Typical periods spent at these energy, loss values were $\Delta t_{2P}=100$ s, $\Delta t_{3P}=600$ s, and $\Delta t_{4P}=1000$ s to acquire about equal statistics for the $2\,^1P$, $3\,^1P$, and $4\,^1P$ coincidence spectra. At $E_0=30$ and 40 eV, we modulated between the $2\,^1P$ and $3\,^1P$ electron energy losses, and (in separate data runs, later) the $2\,^1P$ and $4\,^1P$ electron energy losses. At 80 eV all three energy-loss lines were covered in single data runs. The energy-loss values provided by the spectrometer remained constant (±3 meV over a period of several weeks). With this stability, at the electron energy resolutions mentioned above, we estimated that the relative signal of scattered electrons from $2\,^1P$, $3\,^1P$, and $4\,^1P$ could not vary by more than a percent. Typical times for a single-scattering angle varied from a few hours to about a month. The data were taken at quasirandom values of θ_e, and repeated to check reproducibility or improve statistics.

III. ANALYSIS OF DATA

Typical samples of coincidence spectra produced for electron-photon coincidence experiments involving the $n=3$ and 4 electron energy-loss manifolds are shown in Figs. 3(a)–3(d). The ''tails'' in these spectra are due to contributions from the respective n-singlet states which cascade down to the ground state. These cascades terminate in the ground state via the $2\,^1P$ (for the $n=3$ levels) or $3\,^1P$ (for the $n=4$ levels) levels releasing 58.4- or 53.7-nm photons, which can be detected by our photodetector (see Fig. 4).

A. Analysis of cascades

The contributions of cascades in the $n=3$ and coincidence spectra can be determined by using the procedure described in van Linden van den Heuvell *et al.* [21]. To do this requires a knowledge of the instrumental timing resolution, which is usually assumed to be a Gaussian. However, we noted that in our experiments this is not the case. Observations of our $2\,^1P$ coincidence spectra showed clearly that the peaks were in some cases sharper on the decay side (see Fig. 2 in our previous paper [14]). Thus the conventional analytic form for coincidence peak, using a Gaussian response function for the analyzer [see, e.g., van Linden van den Heuvell *et al.* [21], their Eq. (3.2) and explanatory text] is valid in our case) and another applicable method was needed. The $n=3$ and 4 coincidence spectra were thus numerically deconvoluted for these cascades. The time dependence of such spectra is given numerically by

TABLE I. Relevant singlet-singlet transitions for helium. Transitions labeled with an asterisk lead to trapping into the metastable $2\,^1S$ state, whereas the double asterisk signifies a transition which makes a <1% contribution to the decay. The I.D. symbols refer to Fig. 4.

Transition (LS)	Lifetime	A coefficient (10^8 s^{-1})	Branching ratio (%)	Wavelength (nm)	I.D.
$4\,^1F\rightarrow 3\,^1D$	72.5 ns	0.09478	100	1869.7	Va
$4\,^1D\rightarrow 3\,^1P$	49.5 ns	0.202	74.0	492.2	IVa
$4\,^1D\rightarrow 2\,^1P$	140.6 ns	0.0711	26.0	1908.9	IIa
$4\,^1P\rightarrow 4\,^1S$	17.27 μs	0.000 579	0.024	18 095.0	**
$4\,^1P\rightarrow 3\,^1D$	03.61 μs	0.002 77	0.18	1855.5	Vb
$4\,^1P\rightarrow 3\,^1S$	729.9 ns	0.0137	0.531	1508.4	III
$4\,^1P\rightarrow 2\,^1S$	139.5 ns	0.094 78	3.68	396.5	*
$4\,^1P\rightarrow 1\,^1S$	4.07 ns	2.46	95.39	52.22	Ia
$4\,^1S\rightarrow 3\,^1P$	218 ns	0.094 78	41.20	2113.2	IVb
$4\,^1S\rightarrow 2\,^1P$	152 ns	0.094 78	58.80	504.8	IIb
$3\,^1D\rightarrow 2\,^1P$	15.67 ns	0.638	100	667.8	IIc
$3\,^1S\rightarrow 2\,^1P$	55.2 ns	0.181	100	728.1	IId
$3\,^1P\rightarrow 3\,^1S$	3.953 ns	0.002 53	0.044	7435.1	**
$3\,^1P\rightarrow 2\,^1S$	74.7 ns	0.133 8	2.308	501.6	*
$3\,^1P\rightarrow 1\,^1S$	1.77 ns	5.66	97.648	53.7	1b
$2\,^1P\rightarrow 1\,^1S$	0.55 ns	18.0	100	58.4	1c

$$N_c(t)=N_{nP}\int_{-\infty}^{t} e^{-t'/\tau_{nP}}\mathcal{F}(t')dt' + \sum_{i=1}^{K} N_i\int_{-\infty}^{t} e^{-t'/\tau_i}dt'\int_{-\infty}^{t'} e^{-t''/\tau_{nL}}\mathcal{F}(t'')dt'', \tag{6}$$

where t is the real time, and t' and t'' are dummy (time) variables, and $\mathcal{F}(t)$ is the instrumental time response, derived from the corresponding $2\,^1P$ coincidence spectrum, and made up of a superposition of Gaussians. K is the number of decay cascade channels considered in the deconvolution. The first term in Eq. (6) represents the direct decay photons, whereas the following terms (summation) are due to cascades. The N_{nP} and N_i intensities of the direct and the ith cascade, τ_{nP}, τ_i, and τ_{nL}, are the decay lifetimes of the direct $n\,^1P$, the ith cascade, and the level which terminates the cascade to the ground state. These τ values were taken from Wiese, Smith, and Glennon [22] (see Table I), and the cascade schemes are sketched in Fig. 5. For the $n=3$ manifold we considered the cascades $3\,^1S\rightarrow 2\,^1P\rightarrow 1\,^1S$ ($\tau_{\max}$=55.2 nS) and $3\,^1D\rightarrow 2\,^1P\rightarrow 1\,^1S$ ($\tau_{\max}$=15.67 nS). For the $n=4$ manifold we considered the favored cascades $4\,^1S\rightarrow 2\,^1P\rightarrow 1\,^1S$ ($\tau_{\max}$=152 nS), $4\,^1D\rightarrow 3\,^1P\rightarrow 1\,^1S$ ($\tau_{\max}$=141 nS), and $4\,^1F\rightarrow 3\,^1D\rightarrow 2\,^1P\rightarrow 1\,^1S$ ($\tau_{\max}$=72.5 nS). Here $\tau_{\max}$ is the lifetime of the slowest decay in the cascade (see Table I). We note here that the $n=4$ manifold has more cascading levels than the $n=3$ manifold, but it is simpler to unfold because these cascades are considerably longer than the direct $4\,^1P\rightarrow 1\,^1S$ decay (see table I). N_{nP} and N_i were determined from a nonlinear least-squares fitting of the coincidence spectrum, using the Levenberg-Marquardt method of nonlinear least squares in the *Numerical Recipes in C* software package [23].

B. Branching ratios and quantum efficiency of detector

The resulting areas of the $2\,^1P$ and $n\,^1P$ peaks are corrected for branching ratios, β_γ, according to Eq. (3) as tabulated in Table I. The relative photon detector wavelength efficiency E_γ at 53.7 nm (relative to 58.4 nm was measured by carrying out the same coincidence experiment at $E_0=100$ eV and small ($5°<\theta_e<20°$) scattering angles, and using available theoretical values [9,10,24,25,26] of the ratios of $1\,^1S\rightarrow 2\,^1P$ and $1\,^1S\rightarrow 3\,^1P$ DCS's (which are all in very good agreement in this range). The resulting ratios of relative efficiencies for the 58.4 nm and 53.7 nm VUV radiations were measured to be 1.12 ± 0.02, in very good agreement with measurements taken at the National Institute of Standards and Technology (NIST) for the type of surface (Al_2O_3)

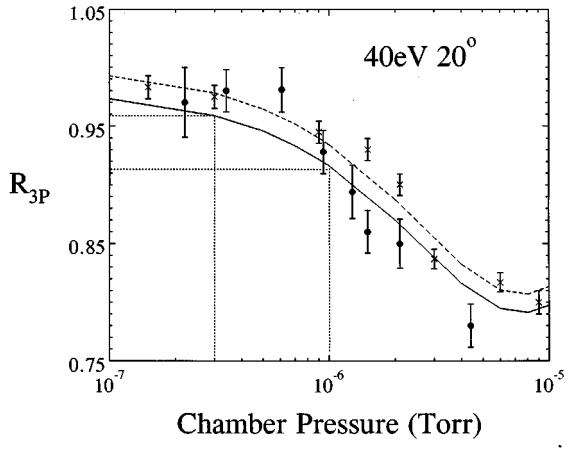

FIG. 5. Effect of radiation trapping on R_{3P}. Legend: ●, experimental values at $E_0=40$ eV and $\theta_e=20°$; ----, analytic model with zero solid angle; —, analytic model with finite solid angle; ×, Monte Carlo simulation. See Sec. III D for details.

used for the first dynode of the detector [27], i.e., 1.13 ± 0.02. We did not repeat such measurements for 52.2 nm ($3\,^1P$ coincidence spectra), and used the NIST data instead, assuming that our detector's efficiency was similar. This is reasonable since these wavelengths are reasonably close. In fact at 52.2 nm the NIST results give the same E_γ ratio for the 58.4–53.7 nm and 58.4–52.2-nm wavelengths. So the value of 1.12 ± 0.02 was adopted for the ratio of our detector E_γ at 58.4–52.2 nm.

C. Polarization efficiency of detector

In preliminary experiments the polarization efficiency of our detector was determined by taking $2\,^1P$ coincidence spectra at several orthogonal values of Φ_γ, i.e., separated by 90°. This was achieved by mounting this detector to an in-vacuum stepper motor. Coincidence spectra at 40 eV and $5° < \theta_e < 30°$ were taken for orthogonal Φ_γ positions of the detector. These coincidence spectra were corrected for the total photon signal. Our detector polarization efficiency was consistently found to be $<1\%$. In later experiments, the stepper motor assembly was removed. This enabled our detector to be moved closer to the collision region to its aforementioned position (Sec. II B).

D. Radiation trapping effects

Finally, the ratios of the areas of the $2\,^1P$ coincidence spectrum and the deconvoluted $n=3$ and 4 spectra need to be corrected for radiation trapping effects. We restricted these measurements to $\theta_e < 30°$, where the coincidence signal was easily obtained and we could repeat R_{nP} ratio measurements relatively quickly. We found that R_{nP} decreased with pressure, independent of the θ_e in the low-pressure domain employed here. A typical plot of the dependence of R_{nP} with pressure is shown in Fig. 5. The theoretical curves are several models of radiation trapping. These models utilized the treatment of light absorption and re-radiation as discussed by Hishikawa *et al.* [28]. The dotted and solid lines are crude models which depend on the *relative* anisotropy of the radiation [$=3/8\pi$ for $\theta_\gamma = 0$ when not trapped; see Eq. (4)] dropping to an isotropic distribution ($=1/4\pi$) when completely trapped. After a collision [whose probability of occurrence $P(l) = e^{-kl}$ depends on the extinction coefficient k and the path length l traveled by the photon in the gas (see Hishikawa *et al.* for details of the dependence of k on the wavelength, the lifetime of the radiation and the density of gas)], the radiation is *isotropically* redistributed. The dotted line is our model for a detector centered at $\theta_\gamma = 0$, with essentially zero solid angle, while the solid line is for our model with a finite solid angle (0.10 sr) centered about $\theta_\gamma = 0$. Typical corrections for the reduction of R_{nP} were in the region of 5–9 % in the range of chamber pressures used here, i.e., 1×10^{-6}–4×10^{-7} torr. Subsequently, we also modeled the radiation trapping using a classical Monte Carlo algorithm (crosses in Fig. 5) similar to that of Hishikawa *et al.* [28], but not including Doppler broadening. We did not correct for the variation of lifetimes with pressure) as this was found negligible in the present range of pressures (evidenced from our Monte Carlo simulation and also observed elsewhere [29]).

The resultant corrected ratios R_{nP} are tabulated together with the respective DCS's (in $\mathrm{cm}^2\,\mathrm{sr}^{-1}$ units) in Tables II(a), II(b), and II(c), and a summary of errors are given in Table III. To obtain the DCS's we normalized our results to recent $2\,^1P$ DCS's, i.e., the weighted average $2\,^1P$ DCSs of Brunger *et al.* [15], Trulhar *et al.* [16], and Cartwright and co-workers [9,24] at 30 and 40 eV. Interpolated and extrapolated values of these DCS's were used which were derived from a polynomial fit to the averaged DCS's. At 80 eV we used the $2\,^1P$ DCS's of Cartwright and co-workers [9,24]. Comparisons with other available data are shown graphically and are discussed next.

IV. DISCUSSION OF RESULTS

A. Ratios R_{nP}

These ratios are plotted in Figs. 6(a)–6(c) for R_{3P} and in Figs. 8(a) and 8(b) for R_{4P}. In Fig. 6(a), we see that the R-matrix theory [6] is not reliable at these energies giving R_{3P} that are almost a factor of 2 lower than our values. The FOMBT [24] provides an excellent shape agreement with our R_{3P} values, but overestimates the value of R_{3P} by about 25% on average. The distorted-wave Born approximation (DWBA) [25] gives good values at small θ_e, but deviates above $\theta_e = 50°$ from our values of R_{3P}. Recent CCC [10] calculations provide the closest agreement in shape and magnitude with our R_{3P} measurements, and in fact are in excellent agreement at $\theta_e > 50°$. The situation at $E_0 = 40$ eV [Fig. 6(b)] is similar to that for $E_0 = 30$ eV, i.e., agreement between experiment and theory is best for the CCC. The CCC is the only theory to display the hump in R_{3P} at around 50° as observed (more strongly) in our experiment. We note that these present CCC results [10] have not yet been tested for convergence, with increasing number of states, regarding these very sensitive R_{nP} values. The FOMBT and DWBA theories give good agreement with experiment for $\theta_e < 40°$. At this E_0 value our R_{3P} measurements are considerably lower than the theoretical results at backward angles. At $E_0 = 80$ eV [Fig. 6(c)], we see that the R_{3P} measurements are essentially flat. The data are restricted to smaller θ_e, i.e., 60° or below, because of the large acquisition times required to obtain reasonable statistics. All theories do equally well in this region, and apart from a disagreement with our R_{3P} at 10° and below overall agreement is very good.

For R_{4P} at $E_0 = 40$ eV and 80 eV [see Figs. 7(a) and 7(b)], we only have comparisons with the FOMBT [9,24] and CCC [10]. The $E_0 = 40$ eV measurements cannot distinguish which of the theories is better, and shows good agreement with the theories. However, at $E_0 = 80$ eV, the measurements are about 30% lower than the theories, although the shape agreement is very good.

B. DCS's

We compare our DCS's for the $1\,^1S \rightarrow 3\,^1P$ transition in Figs. 8(a), 8(b), and 8(c). These DCS are obtained from our R_{3P} values using a weighted average of available experimental $1\,^1S \rightarrow 2\,^1P$ DCS's from the work of Refs. [9], [15], [16], and [24]. Comparisons of the DCS's at $E_0 = 30$ eV give excellent agreement with the CCC within the combined errors of our R_{3P} values and the averaged DCS's. The FOMBT

TABLE II. Summary of present results at (a) $E_0 = 30$ eV, (b) 40 eV, and (c) 80 eV. For additional details, see text.

(a) 30-eV data

Angle (deg)	$2\,^1P$ DCS	Error	Ratio $2\,^1P$:$3\,^1P$	Error	$3\,^1P$ DCS	Error
5	5.2×10^{-18}	6.3×10^{-19}	6.4	0.5	8.1×10^{-19}	1.2×10^{-19}
10	3.9×10^{-18}	6.3×10^{-19}	5.9	0.4	6.7×10^{-19}	1.2×10^{-19}
15	3.2×10^{-18}	5.1×10^{-19}	5.8	0.4	5.5×10^{-19}	9.7×10^{-20}
20	2.4×10^{-18}	3.9×10^{-19}	5.3	0.4	4.6×10^{-19}	8.2×10^{-20}
25	1.9×10^{-18}	3.0×10^{-19}	5.3	0.5	3.6×10^{-19}	6.4×10^{-20}
30	1.4×10^{-18}	2.2×10^{-19}	4.4	0.5	3.1×10^{-19}	6.1×10^{-20}
40	5.7×10^{-19}	9.3×10^{-20}	3.9	0.5	1.5×10^{-19}	2.9×10^{-20}
50	2.9×10^{-19}	4.9×10^{-20}	3.7	0.5	7.9×10^{-20}	1.7×10^{-20}
60	1.5×10^{-19}	2.7×10^{-20}	3.8	0.6	4.0×10^{-20}	9.2×10^{-21}
65	1.2×10^{-19}	2.3×10^{-19}	3.8	0.5	3.2×10^{-20}	6.0×10^{-20}
70	1.1×10^{-19}	2.1×10^{-20}	4.1	0.6	2.7×10^{-20}	6.3×10^{-21}
80	9.3×10^{-20}	1.8×10^{-20}	4.8	0.6	1.9×10^{-20}	4.4×10^{-21}
90	8.9×10^{-20}	1.7×10^{-20}	4.8	0.6	1.8×10^{-20}	4.1×10^{-21}
100	8.4×10^{-20}	1.6×10^{-20}	4.5	0.6	1.9×10^{-20}	4.3×10^{-21}
110	6.7×10^{-20}	1.3×10^{-20}	5.0	0.5	1.3×10^{-20}	2.9×10^{-22}
120	6.8×10^{-20}	1.3×10^{-20}	4.7	0.6	1.4×10^{-20}	3.3×10^{-21}
125	6.5×10^{-20}	1.3×10^{-20}	4.3	0.7	1.5×10^{-20}	3.8×10^{-21}

(b) 40-eV data

Angle (deg)	$2\,^1P$ DCS	Error	Ratio $2\,^1P$:$3\,^1P$	Error	$3\,^1P$ DCS	Error	Ratio $2\,^1P$:$4\,^1P$	Error	$4\,^1P$ DCS	Error
5	1.5×10^{-17}	3.6×10^{-18}					16.2	2.2	9.5×10^{-19}	2.5×10^{-19}
10	1.3×10^{-17}	2.6×10^{-18}	5.6	0.5	2.4×10^{-18}	5.1×10^{-19}	14.7	1.9	9.0×10^{-19}	2.1×10^{-19}
15	9.0×10^{-18}	1.8×10^{-18}	5.4	0.3	1.7×10^{-18}	3.5×10^{-19}	13.4	1.8	6.7×10^{-19}	1.6×10^{-19}
20	4.6×10^{-18}	7.3×10^{-20}	5.0	0.3	9.2×10^{-19}	1.6×10^{-19}	14.8	2.0	3.1×10^{-19}	6.4×10^{-20}
25	2.8×10^{-18}	5.6×10^{-19}	4.2	0.5	6.7×10^{-19}	1.5×10^{-19}	12.2	1.6	2.3×10^{-19}	5.5×10^{-20}
30	1.6×10^{-18}	2.0×10^{-19}	4.4	0.4	3.8×10^{-19}	6.0×10^{-20}	13.5	1.8	1.2×10^{-19}	2.2×10^{-20}
35	9.5×10^{-19}	1.9×10^{-20}					11.4	2.7	8.3×10^{-20}	2.0×10^{-20}
40	5.9×10^{-19}	7.6×10^{-20}	4.9	0.4	1.2×10^{-19}	1.9×10^{-20}	12.0	1.8	5.0×10^{-20}	9.8×10^{-21}
50	2.8×10^{-19}	3.4×10^{-20}	4.8	0.6	5.8×10^{-20}	1.0×10^{-20}	11.5	1.6	2.4×10^{-20}	4.5×10^{-21}
60	1.7×10^{-19}	2.2×10^{-20}	5.3	0.5	3.3×10^{-20}	5.1×10^{-21}				
65	1.6×10^{-19}	3.1×10^{-20}	4.6	0.3	3.3×10^{-20}	7.1×10^{-21}				
70	1.4×10^{-19}	1.5×10^{-20}	3.6	0.5	3.8×10^{-20}	6.3×10^{-21}				
80	1.2×10^{-19}	1.0×10^{-20}	3.3	0.4	3.5×10^{-20}	4.9×10^{-21}				
90	9.6×10^{-20}	9.1×10^{-21}	3.4	0.5	2.8×10^{-20}	5.0×10^{-21}				
100	9.0×10^{-20}	8.3×10^{-21}	2.4	0.4	3.7×10^{-20}	6.7×10^{-21}				
110	7.6×10^{-20}	7.4×10^{-21}	2.7	0.4	2.8×10^{-20}	5.2×10^{-21}				
120	6.6×10^{-20}	8.0×10^{-21}	2.8	0.3	2.4×10^{-20}	4.1×10^{-21}				
125	6.4×10^{-20}	1.3×10^{-20}	2.4	0.4	2.7×10^{-20}	7.0×10^{-21}				
130	6.0×10^{-20}	1.2×10^{-20}	2.8	0.3	2.2×10^{-20}	5.1×10^{-21}				

(c) 80-eV data

Angle (deg)	$2\,^1P$ DCS	Error	Ratio $2\,^1P$:$3\,^1P$	Error	$3\,^1P$ DCS	Error	Ratio $2\,^1P$:$4\,^1P$	Error	$4\,^1P$ DCS	Error
5	5.2×10^{-17}	8.9×10^{-18}	4.1	0.3	1.3×10^{-17}	2.5×10^{-18}	10.7	1.4	4.9×10^{-18}	1.1×10^{-18}
10	2.6×10^{-17}	4.4×10^{-18}	3.5	0.4	7.5×10^{-18}	1.5×10^{-18}	9.6	1.2	2.7×10^{-18}	5.8×10^{-19}
15	1.1×10^{-17}	1.8×10^{-18}	3.8	0.5	2.7×10^{-18}	6.1×10^{-19}	9.0	1.3	1.2×10^{-18}	2.6×10^{-19}
20	4.3×10^{-18}	7.3×10^{-19}	3.9	0.5	1.1×10^{-18}	2.4×10^{-19}	7.4	1.1	5.8×10^{-19}	1.3×10^{-19}
30	7.7×10^{-19}	1.3×10^{-19}	3.4	0.4	2.3×10^{-19}	4.9×10^{-20}	6.0	0.9	1.3×10^{-19}	2.9×10^{-20}
40	2.3×10^{-19}	3.9×10^{-20}	3.5	0.6	6.6×10^{-20}	1.6×10^{-20}	6.4	1.1	3.6×10^{-20}	8.6×10^{-21}
50	1.2×10^{-19}	2.0×10^{-20}	3.5	0.5	3.5×10^{-20}	7.8×10^{-21}	5.9	1.2	2.0×10^{-21}	5.4×10^{-21}
60	8.0×10^{-20}	1.4×10^{-20}	3.8	0.5	2.1×10^{-20}	4.6×10^{-21}				

TABLE III. Summary of errors of present work. Errors are one standard deviation.

Source of error	$3\,^1P$	$4\,^1P$
Detection efficiency	5%	5%
Analyzer transmission	5%	5%
Statistics and fitting to feature	5–20 %	8–25 %
$2\,^1P$ DCS error	7–20 %	10–20 %
Radiation trapping	5%	5%
Total error	16–26 %	20–30 %

shows good agreement with the measurements at $\theta_e < 40°$, but then drops down by a factor of 2. The DWBA and R-matrix theories both do not do so well, giving DCS's that are too high. The DWBA extrapolates to the measured DCS's at small $\theta_e < 15°$. The disagreement with the R matrix demonstrates that in this case it cannot be valid for E_0 values in the range of this experiment. To provide added tests for the R matrix at $E_0 < 30$ eV is difficult with our arrangement, because for $E_0 < 30$ eV the DCS's of the $n\,^1P$ features are lower, and also because our experiment becomes prone to uncertainty in the relative transmission of the electron analyzer. Finally at $E_0 = 30$ eV, comparison with the present semiempirical DCS's and the DCS's of Chutjian and Thomas [5] shows very good agreement.

The DWBA is recognized as an intermediate-energy theory, and is not expected to be valid at the value of $E_0 = 30$ eV; however, at $E_0 = 40$ eV [Fig. 8(b)] the DWBA [25] is in reasonable agreement with experimental DCS's, being higher than our experimental DCS's. Here, the CCC [10] gives the best agreement with our DCS's. Very good agreement with the DCS's of Chutjian and Thomas is observed, but at $\theta_e > 60°$ the present experimental DCS's are somewhat higher. At $E_0 = 80$ eV, agreement between the present DCS's, the CCC [10], and the FOMBT [9,24] is very good, especially with the CCC which goes through all the present data points. Agreement with the DWBA [25] is not as good in the region of $10° < \theta_e < 60°$.

In Figs. 9(a) and 9(b), we compare the present $1\,^1S \rightarrow 4\,^1P$ DCSs with available DCS's from the FOMBT [9,24] and the CCC [10] at $E_0 = 40$ and 80 eV. Both theories agree very well with our results, but the CCC gives better agreement with the present DCSs. At 80 eV, agreement with both the FOMBT and CCC is very good.

C. n independence of the electron-impact excitation of $1\,^1S \rightarrow n\,^1P$ transitions

For the excited states of helium the quantum defect μ_n for the nth level is obtained using the Heisenberg method [30]. For helium, $\mu_n = -0.0222$, -0.0242, and -0.0247 for $n = 2$, 3, and 4, respectively, i.e., very small. Thus the DCS scaling law [$\propto (n-\mu_n)^{-3}$; see Sec. I] predicts R_{nP} ($n = 3$ and 4) ratios of 3.34 and 7.88. For a similar ratio

$$R'_{nP} = \frac{d\sigma/d\Omega(E_0,\theta_e)_{3P}}{d\sigma/d\Omega(E_0,\theta_e)_{nP}}, \tag{7}$$

the scaling law predicts values of R'_{nP} ($n = 2$ and 4) of 0.30 and 2.36, respectively. Any departure of our experimental values of R_{nP} or R'_{nP} from these predictions indicates that one or both DCS's involved in these ratios is not following the scaling law. From Figs. 6 and 7, we see that this n independence is not reached at $E_0 = 40$ eV, because R_{3P} monotonically decreases with θ_e, dropping to 2.6 ± 0.4, i.e., well below the theoretical n-independence value of 3.34. At $E_0 = 40$ eV we find that the average of R_{4P} values for $\theta_e > 10°$ is considerably higher (i.e., 12.5 ± 2) and somewhat outside of error bars from the theoretical 7.88 value. At $E_0 = 80$ eV we observe that the n independence may have been reached for angles $\theta_e > 10°$ using R_{3P} and R_{4P}. For R_{3P}

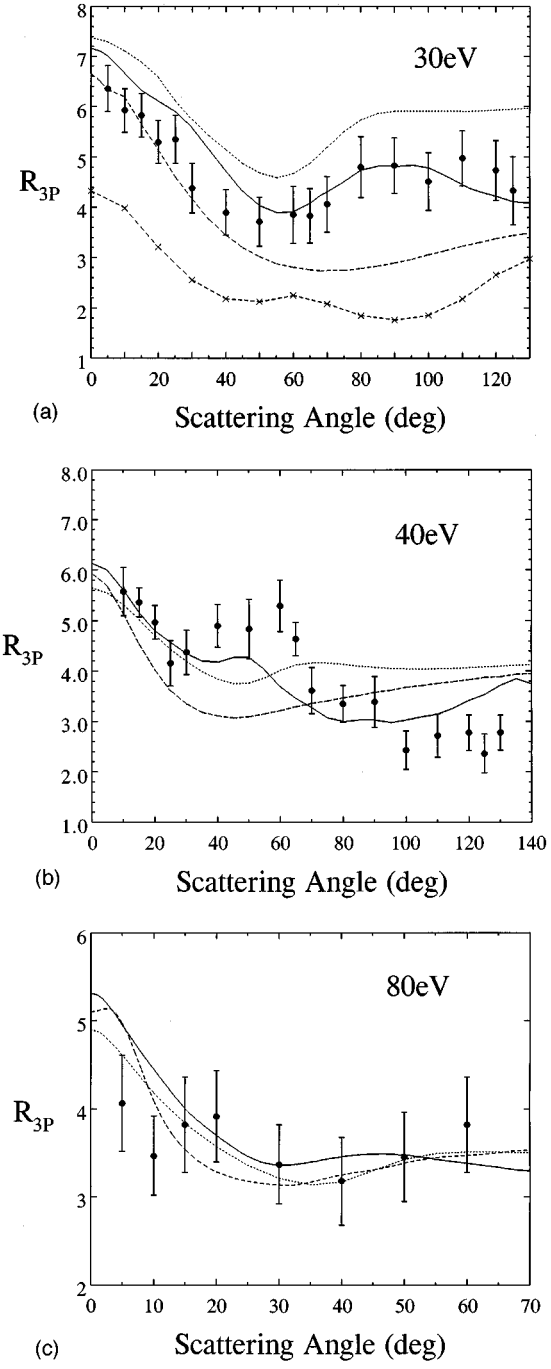

FIG. 6. Ratios R_{3P} at (a) 30-eV, (b) 40-eV, and (c) 80-eV impact energies. Legend: -, experiment; ●, present work. Theory: ----, DWBA [25]; ...., FOMBT [9,24]; ---, R matrix [6]; —, CCC [10].

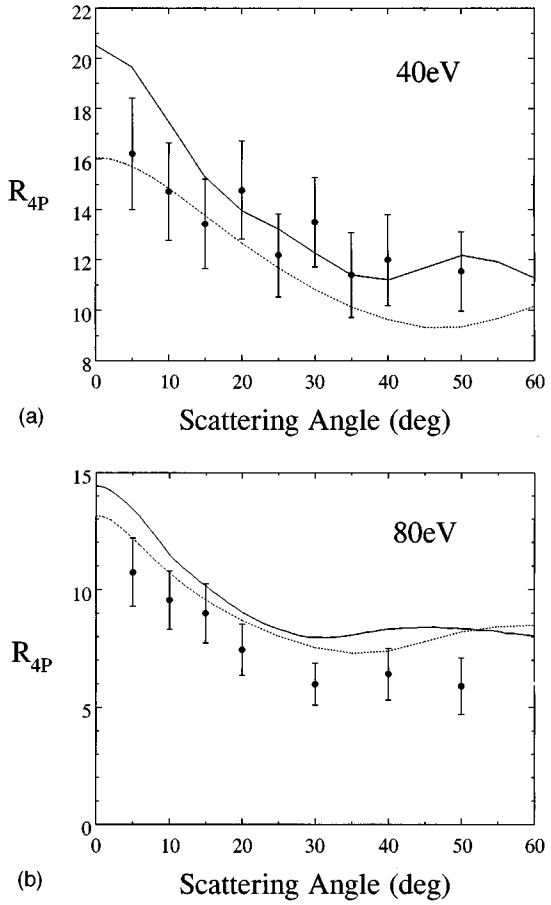

FIG. 7. Ratios R_{4P} at (a) 40-eV and (b) 80-eV impact energies. Legend: ●, present work. Theory: ...., FOMBT [24]; —, CCC [10].

we obtain an average value of 3.6 ± 0.5, in very good agreement with the n-independence value of 3.34. Turning to R_{4P} at $E_0=80$ eV, our $\theta_e>10°$ values average a little lower (but inside our standard deviation errors) than the n-independent value of 7.88, i.e., 6.9 ± 1.1 when we consider our data at $\theta_e>10°$. Comparing the ratio of DCS's R'_{4P} from our Tables II(b) and II(c), we see that at 40 eV R'_{4P} is flat across the whole range of measurements. So taking the average of all the data points we obtain a DCS $R'_{4P}=2.70\pm0.44$, in very good agreement with the n-independent ratio. At 80 eV for this ratio we obtain a lowering of this ratio for $\theta_e>10°$ from 2.6 ± 0.42 to 1.8 ± 0.42. This again is just below of the theoretical value of 2.36. The above measurements thus provide strong support that at larger θ_e ($>10°$), for $n=3$ and 4 at $E_0=40$ eV and above the n independence of the DCS's is met, whereas for $n=2$ one needs to go to $E_0>40$ eV and $\theta_e>10°$.

A semiclassical interpretation of the lowering of this ratio as θ_e increases could be that at smaller θ_e the interactions are long range, and so the DCS's are strongly influenced by the large-r dependences of the wave functions, i.e., now n-independence effects are not dominant. At larger angles, shorter-range effects due to the penetration of the scattering electron into the target atom will result in n-independent effects dominating.

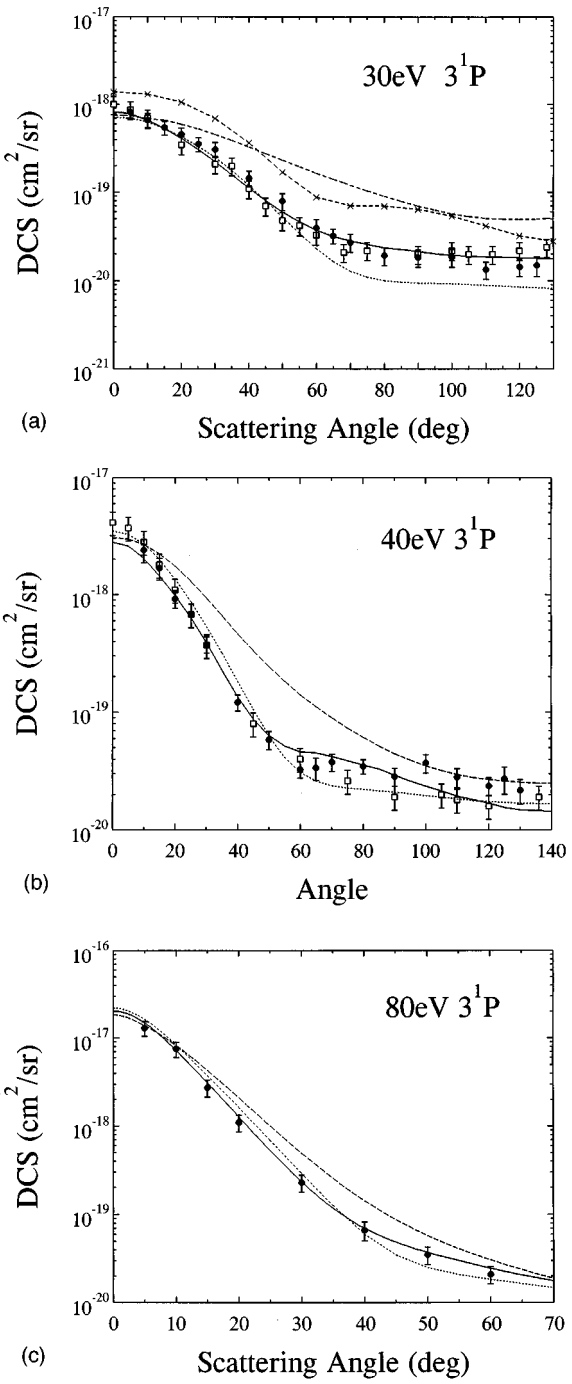

FIG. 8. Normalized DCSs for the $1\,^1S\rightarrow3\,^1P$ transition at (a) 30-eV, (b) 40-eV, and (c) 80-eV impact energies. The legend is the same as in Fig. 6, except open squares are $1\,^1S\rightarrow3\,^1P$ DCS's of Chutjian and Thomas [5].

D. Cascade excitations

Figures 10(a) and 10(b) show examples of the relative contributions of the $3\,^1D$ and $3\,^1S$ excitations at $E_0=40$ eV with respect to the $3\,^1P$ excitation. These relative contributions cannot be converted into DCS's, because the angular distribution function for the $n\,^1S$ and $n\,^1D$ states has a different symmetry from that for the $n\,^1P$ states, and requires that detailed information about the angular distribution of the excited state needs to be known, before the DCS's of the

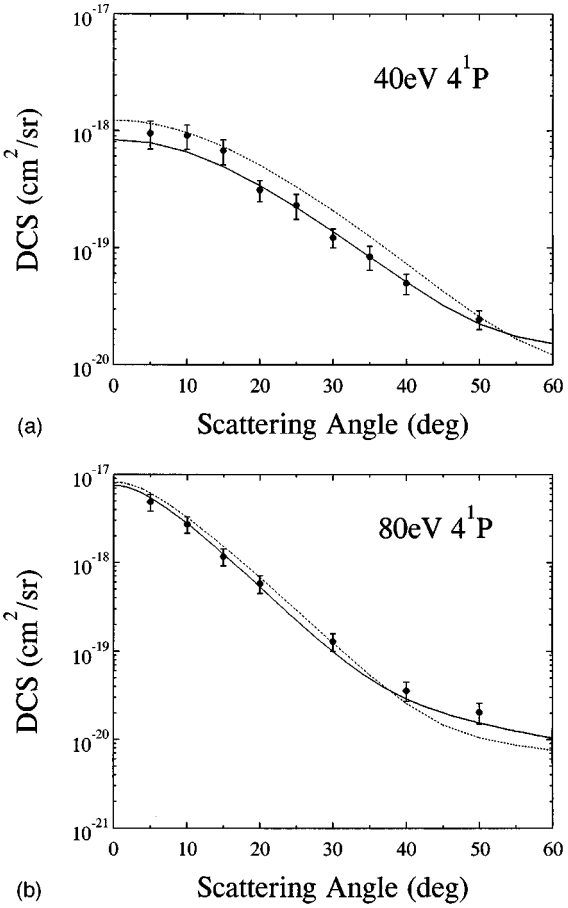

FIG. 9. Same as Fig. 8, but for the $1\,^1S \rightarrow 4\,^1P$ transition at (a) 40-eV and (b) 80-eV impact energies. Legend: ●, present work. Theory: ...., FOMBT [24]; —, CCC [10].

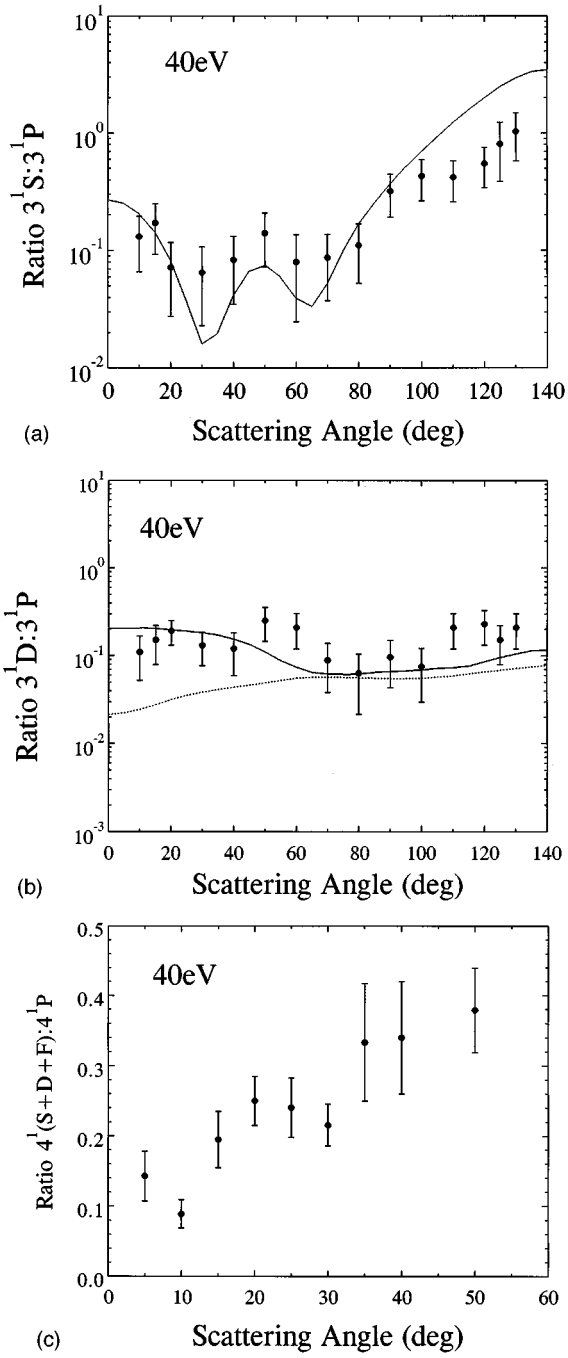

FIG. 10. Cascade contributions to the coincidence spectra at $E_0 = 40$ eV. (a) $3\,^1S$ contribution as a fraction of $3\,^1P$. (b) $3\,^1D$ contribution as a fraction of $3\,^1P$. (c) Summed cascade contributions as a fraction of the $4\,^1P$. Legend: ●, present work. theory: ...., FOMBT [9,24]; —, CCC [10].

$n\,^1S$ and $n\,^1D$ states can be extracted from present-type coincidence experiments. We thus show the $3\,^1D$ and $3\,^1S$ coincidence signal ratios relative to the $3\,^1P$ state at $E_0 = 40$ eV. Comparison is made with the CCC [10] and the FOMBT [9,24] DCS ratios for these states. As can be observed, the angular (θ_e) dependence of the $3\,^1S$:$3\,^1P$ ratio is different from the $3\,^1D$:$3\,^1P$ ratio. Whereas the $3\,^1D$:$3\,^1P$ ratio remains relatively constant between 0.1 and 0.2, the $3\,^1S$:$3\,^1P$ ratio goes up to 0.8. Comparison with theory shows that the $3\,^1D$:$3\,^1P$ ratios given by the CCC are reasonable, but those of the FOMBT are too low. These effects are also observed at $E_0 = 30$ eV and at 80 eV with approximately the same magnitudes. For the $n = 4$ levels, the situation is clear. The DCSs of $4\,^1S$, $4\,^1D$, and $4\,^1F$ cannot be clearly differentiated from each other. This is due to a data analysis problem. It is difficult to differentiate the coincidence spectrum contributions from $4\,^1S$, $4\,^1D$, and $4\,^1F$ because of their relatively similar lifetimes in comparison to that of direct $4\,^1P$ (Table II). So we have grouped all these cascades as a single unit. This yields a more defined profile which is plotted in Fig. 10(c) for $E_0 = 40$ eV. It is observed that the overall cascade contributions to the coincidence spectra increases as θ_e increases.

V. CONCLUSIONS

We have described the implementation of a useful experimental method to determine DCS's of the 3,4 ^1P states of helium which cannot be resolved using conventional EELS. This is possible by application of the electron-photon coincidence method in the VUV and time analysis of the coincidence spectra to ''resolve'' the $n\,^1P$ contributions. The present $3\,^1P$ DCS's are found to be in good agreement with the earlier semiempirical DCS's of Chutjian and Thomas [5]. Very good agreement is obtained with the CCC method [10] and with the FOMBT [24]. Agreement with the DWBA [25], however is, not as good as the CCC and FOMBT. Extending these measurements to $4\,^1P$, we find excellent agreement with the CCC and FOMBT. We also find reasonable experi-

mental evidence to indicate that the $3\,^1P$ and $4\,^1P$ n independence suggested by Csanak and Cartwright [11] is applicable at $E_0=40$ and 80 eV for $\theta_e>10°$. However, for the $2\,^1P$ state, the n-independence model is applicable at $E_0=80$ eV.

ACKNOWLEDGMENTS

This work was supported by the National Science Foundation, under Grants Nos. NSF-RUI-PHY-9205423 and NSF-RUI-PHY-9511549. The generous donation of equipment by Dr. S. Trajmar is very gratefully acknowledged. Discussions with Dr. G. Csanak, Dr. S. Trajmar, Dr. T. J. Gay, Dr. E. J. Mansky, Dr. P. Hammond, Dr. D. Madison, Dr. I. Bray, Dr. A. Crowe, Dr. J. F. Williams, and Dr. J. Slevin are gratefully appreciated. The technical expertise of CSUF technicians H. Fabris, N. Nitzberg, T. Timpe, and D. Parsons is also acknowledged. Added input for this work came from L. Bubion and D. Bordelon.

[1] S. Trajmar and I. Kanik, in *Atomic and Molecular Processes in Fusion Edge Plasmas*, edited by R. K. Janev (Plenum, New York, 1995), pp. 31–58.
[2] S. Trajmar, J. M. Ratliff, G. Csanak, and D. C. Cartwright, Z. Phys. D **22**, 457 (1992).
[3] N. Andersen, J. W. Gallagher, and I. V. Hertel, Phys. Rep. **165**, 1 (1988).
[4] K. Becker, A. Crowe, and J. W. McConkey, J. Phys. B Opt. Phys. **25**, 3885 (1992).
[5] A. Chutjian and L. D. Thomas, Phys. Rev. A **11**, 1583 (1975).
[6] W. C. Fon, K. A. Berrington, and A. E. Kingston, J. Phys. B Opt. Phys. **21**, 2961 (1988).
[7] G. J. Ferland, Astrophys. J. **310**, L67 (1987); B. E. J. Pagel and E. A. Simonson, Rev. Mex. Astron. Astrophys. **18**, 153 (1989).
[8] W. C. Fon and K. P. Lim, J. Phys. B **23**, 3691 (1990); P. J. M. Sawey, K. A. Berrington, P. G. Burke, and A. E. Kingston, *ibid*. **23**, 3885 (1990).
[9] D. C. Cartwright, G. Csanak, S. Trajmar, and D. F. Register, Phys. Rev. A **45**, 1602 (1992); D. C. Cartwright, G. Csanak, and S. Trajmar, *ibid*. **45**, 1625 (1992).
[10] D. V. Fursa and I. Bray, Phys. Rev. A **52**, 1279 (1995); I. Bray (private communication).
[11] D. C. Cartwright and G. Csanak, Phys. Rev. A **34**, 93 (1986).
[12] V. Bubelev, D. H. Madison, I. Bray, and A. T. Stelbovics, J. Phys. B **28**, 4619 (1996); V. Bubelev and D. H. Madison, *ibid*. **29**, 1737 (1996); V. Bubelev, D. H. Madison, and M. A. Pinkerton, *ibid*. **29**, 1751 (1996).
[13] P. Hammond, M. A. Khakoo, and J. W. McConkey, Phys. Rev. A **36**, 5127 (1987).
[14] M. A. Khakoo, D. Roundy, and F. Rugamas, Phys. Rev. Lett. **75**, 41 (1995).
[15] M. J. Brunger, I. E. McCarthy, K. Ratnavelu, P. J. O. Teubner, A. M. Weigold, Y. Zhou, and L. J. Allen, J. Phys. B **23**, 1325 (1991).
[16] D. G. Trulhar, S. Trajmar, W. Williams, S. Ormonde, and B. Torres, Phys. Rev. A **8**, 1602 (1973).
[17] J. Slevin, Rep. Prog. Phys. **47**, 461 (1984).
[18] M. A. Khakoo, T. Jayaweera, S. Wang, and S. Trajmar, J. Phys. B **26**, 4845 (1993).
[19] J. Nickel, P. W. Zetner, G. Shen, and S. Trajmar, J. Phys. E **22**, 730 (1989).
[20] M. A. Khakoo, C. E. Beckmann, S. Trajmar, and G. Csanak, J. Phys. B **27**, 3159 (1994).
[21] H. B. van Linden van den Heuvell, E. M. van Gasteren, J. van Eck, and H. G. M. Heideman, J. Phys. B **16**, 1619 (1983).
[22] W. Wiese, M. W. Smith, and B. M. Glennon, *Atomic Transition Probabilities*, Natl. Bur. Stand. (U.S.) (U.S. GPO, Washington, D.C., 1966), Vol. 1.
[23] W. H. Press, B. P. Flannery, S. A. Teukolsky, and W. T. Vetterling, *Numerical Recipes in C* (Cambridge University Press, New York, 1988).
[24] D. C. Cartwright (private communication).
[25] K. Bartschat and D. H. Madison, J. Phys. B **20**, 153 (1988); D. H. Madison (private communication).
[26] I. McCarthy (private communication).
[27] L. Randall Canfield and Nils Swanson, J. Res. Natl. Bur. Stand. **92**, 97 (1987).
[28] A. Hishikawa, H. Mizuno, M. Tani, and R. Okasaka, J. Phys. B **25**, 3419 (1992).
[29] J. F. Williams, R. Hippler, J. B. Wang, A. G. Micosza, and A. B. Wedding, Phys. Rev. Lett. **69**, 757 (1992); A. G. Micosza, R. Hippler, J. B. Wang, J. F. Williams, and A. B. Wedding, J. Phys. B **27**, 1429 (1994).
[30] H. A. Bethe and E. E. Salpeter, *Quantum Mechanics of One- and Two-Electron Atoms* (Springer-Verlag, New York, 1957), p. 136.